Monthly Notices of the ROYAL ASTRONOMICAL SOCIETY

MNRAS **463,** 1724–1739 (2016) doi:10.1093/mnras/stw2097
Advance Access publication 2016 August 22

The BLUEDISK survey: molecular gas distribution and scaling relations in the context of galaxy evolution

D. Cormier,[1⋆] F. Bigiel,[1] J. Wang,[2] J. Pety,[3] A. Usero,[4] S. Roychowdhury,[5] D. Carton,[6] J. M. van der Hulst,[7] G. I. G. Józsa,[8] M. González-García[9] and A. Saintonge[10]

[1]*Zentrum für Astronomie der Universität Heidelberg, Institut für theoretische Astrophysik, Albert-Ueberle-Str. 2, D-69120 Heidelberg, Germany*
[2]*CSIRO Astronomy and Space Science, Australia Telescope National Facility, PO Box 76, Epping, NSW 1710, Australia*
[3]*Institut de Radioastronomie Millimétrique, 300 Rue de la Piscine, F-38406 Saint Martin d'Hères, France*
[4]*Observatorio Astronómico Nacional (IGN), C/ Alfonso XII 3, E-28014 Madrid, Spain*
[5]*Max-Planck-Institut für Astrophysik, Karl-Schwarzschild-Str. 1, D-85748 Garching, Germany*
[6]*Leiden Observatory, Leiden University, PO Box 9513, NL-2300 RA Leiden, the Netherlands*
[7]*Kapteyn Astronomical Institute, University of Groningen, PO Box 800, NL-9700 AV Groningen, the Netherlands*
[8]*SKA South Africa, 3rd Floor, The Park, Park Road, Pinelands, 7405, South Africa*
[9]*Instituto de Astrofísica de Andalucía IAA-CSIC, Glorieta de la Astronomía s/n, E-18008 Granada, Spain*
[10]*Department of Physics and Astronomy, University College London, Gower Place, London WC1E 6BT, UK*

Accepted 2016 August 18. Received 2016 August 18; in original form 2016 June 10

ABSTRACT

One of the key goals of the BLUEDISK survey is to characterize the impact of gas accretion in disc galaxies in the context of galaxy evolution. It contains 50 disc galaxies in the stellar mass range 10^{10}–10^{11} $M_{\odot}$, of which half are bluer and more H I-rich galaxies than their H I-normal (control) counterparts. In this paper, we investigate how ongoing disc growth affects the molecular gas distribution and the star formation efficiency in these galaxies. We present ^{12}CO observations from the IRAM 30-m telescope in 26 galaxies of the BLUEDISK survey. We compare the amount and spatial distribution of the molecular gas to key quantities such as atomic gas, stellar mass and surface density, star formation rate (SFR) and metallicity. We analyse the SFR per unit gas (SFR/H I and SFR/H_2) and relate all those parameters to general galaxy properties (H I-rich/control disc, morphology, etc.). We find that the H I-rich galaxies have similar H_2 masses as the control galaxies. In their centres, H I-rich galaxies have lower H_2/H I ratios and marginally shorter molecular gas depletion times. However, the main differences between the two samples occur in the outer parts of the discs, with the H I-rich galaxies having slightly smaller CO discs (relative to the optical radius R_{25}) and steeper CO and metallicity gradients than the control galaxies. The ongoing accretion of H I at large radii has thus not led to an appreciable growth of the CO discs in our sample. Based on depletion times, we estimate that this gas will contribute to star formation on time-scales of at least 5 Gyr.

Key words: galaxies: evolution – galaxies: spiral – galaxies: star formation – radio lines: ISM.

1 INTRODUCTION

At all redshifts, the star formation activity and the amount of stars in most galaxies are related and define what is known as the main sequence of galaxies (e.g. Elbaz et al. 2007; Noeske et al. 2007). However, for present-day galaxies to maintain their star formation at the observed level, they need to be replenished in gas (e.g. Kennicutt 1983; Erb 2008; Hopkins, McClure-Griffiths & Gaensler 2008; Bauermeister, Blitz & Ma 2010). There is growing evidence of large atomic gas reservoirs in the outer parts of galaxies (e.g. Bigiel et al. 2010a,b), due to external accretion or galactic fountains (e.g. Sancisi et al. 2008; Catinella et al. 2010). Galaxies with significant excess atomic gas feature bluer, younger, and more metal-poor outer discs (Moran et al. 2010, 2012; Wang et al. 2010). This supports an 'inside-out' picture of galactic disc formation, in which the inner part forms first and infalling cool gas in the outer part then contributes to the build-up of the disc.

⋆ E-mail: diane.cormier@zah.uni-heidelberg.de

Table 1. Properties of our selected galaxy sample.

SDSS name	Galaxy ID	Dist. (Mpc)	Incl. (°)	PA (°)	D_{25} (arcmin)	$NUV-r$ (mag)	log $M_\star$ (log $M_\odot$)	log M(H I) (log $M_\odot$)	Morphology
BLUEDISK Galaxies observed with HERA									
J081422.02+391504.8	ID1$^{\text{H I-rich}}$	121	34	100	1.27	2.37	10.4	10.1	SBc face-on
J082846.72+403957.0	ID2$^{\text{H I-rich}}$	107	66	111	1.36	3.02	10.6	9.9	Sb
J083706.51+412722.8	ID3$^{\text{control}}$	128	37	73	0.82	2.44	10.4	9.9	Sc
J083833.99+304755.2	ID4$^{\text{H I-rich}}$	112	62	109	1.48	2.36	10.6	10.3	Sc, lopsided
J084916.39+360711.3	ID5$^{\text{H I-rich}}$	110	21	−8	1.09	2.01	10.3	10.2	Sab face-on
J084922.57+364237.5	ID6$^{\text{H I-rich}}$	109	52	61	1.73	2.94	10.8	10.3	SBb, one arm
J090842.68+444838.0	ID8$^{\text{H I-rich}}$	117	48	54	1.10	2.19	10.3	10.2	Sc, clumpy
J091458.31+512139.8	ID9$^{\text{control}}$	120	63	105	1.22	2.93	10.8	9.9	SB, clumpy
J093225.04+572858.4	ID10$^{\text{control}}$	129	37	25	1.00	2.43	10.9	10.0	SBa
J101054.38+455701.3	ID11$^{\text{control}}$	105	56	−4	1.23	2.74	10.6	9.7	Sb
J090842.68+444838.0	ID14$^{\text{H I-rich}}$	104	61	159	1.46	3.25	10.8	10.1	Sa
J114859.46+350057.7	ID15$^{\text{H I-rich}}$	93	51	22	1.86	2.43	10.8	10.4	Sab, two arms
J125203.54+514048.2	ID16$^{\text{H I-rich}}$	119	40	19	0.90	2.01	10.3	10.0	Sc, clumpy
J130713.58+580806.1	ID17$^{\text{H I-rich}}$	120	44	17	1.02	2.85	10.7	10.3	Sb face-on
J143759.94+400622.3	ID20$^{\text{H I-rich}}$	114	52	2	1.29	1.55	10.2	10.1	Sc, clumpy
BLUEDISK Galaxies observed with EMIR									Pair
J080240.65+343117.2	ID27$^{\text{control}}$	126	39	−77	0.62	2.90	10.3	9.3	ID3$^{\text{control}}$
J082914.91+553122.8	ID29$^{\text{excluded}}$	112	64	95	1.25	2.90	10.5	10.4	ID4$^{\text{H I-rich}}$
J091645.74+454844.1	ID31$^{\text{excluded}}$	114	52	−38	0.75	2.68	10.2	10.1	ID20$^{\text{H I-rich}}$
J092609.43+491836.7	ID33$^{\text{control}}$	118	58	−62	1.12	3.99	10.7	9.2	ID9$^{\text{control}}$
J095740.85+451531.2	ID35$^{\text{H I-rich}}$	106	71	−62	1.28	3.32	10.6	9.9	ID15$^{\text{H I-rich}}$
J101511.43+564019.5	ID37$^{\text{control}}$	114	31	−80	1.05	2.81	10.4	9.7	ID5$^{\text{H I-rich}}$
J111415.25+340915.8	ID40$^{\text{control}}$	119	39	103	0.73	2.83	10.4	9.7	ID1$^{\text{H I-rich}}$
J122139.99+405056.4	ID41$^{\text{control}}$	130	31	−23	0.91	3.45	10.8	–	ID10$^{\text{control}}$
J133329.90+403146.8	ID43$^{\text{control}}$	118	48	162	0.76	2.74	10.3	9.6	ID16$^{\text{H I-rich}}$
J134100.24+422553.1	ID44$^{\text{control}}$	122	51	40	1.03	3.34	10.8	9.3	ID17$^{\text{H I-rich}}$
J161731.80+311140.1	ID47$^{\text{H I-rich}}$	105	54	199	1.10	2.91	10.5	10.0	ID11$^{\text{control}}$

Notes. Parameters taken from Wang et al. (2013): name, identification number, luminosity distance, diameter of the g-band 25 mag arcsec^{-2} isophote, inclination, position angle of the major axis, stellar mass, H I mass, and morphology. The position angle is measured from SDSS data, with respect to west. The distance is the luminosity distance, calculated from the redshift assuming $H_0 = 70$ km s^{-1} Mpc^{-1}, $\Omega_M = 0.3$, $\Lambda_0 = 0.7$, $q_0 = -0.55$. The upper script next to the ID indicates which group the galaxy belongs to (H I-rich, control, excluded; where excluded galaxies are multisource systems, see Wang et al. 2014).

How specifically this gas influences star formation, disc growth, and galaxy evolution remains unclear. In this frame, knowledge of the molecular gas content is necessary to better understand the link between the accreted atomic gas and star formation occurring predominantly in the centre of the disc. Surveys of the atomic and molecular reservoirs in nearby, stellar-mass-selected galaxies such as GASS (Catinella et al. 2010) and COLD GASS (Saintonge et al. 2011a) have shed light on the global gas content of massive galaxies. Catinella et al. (2010) showed that most galaxies lie on a tight plane linking the atomic gas content with the UV/optical colours and stellar mass surface densities. For galaxies with an excess of atomic gas, i.e. above that plane, Saintonge et al. (2011a) do not find differences in their molecular gas mass. However, only global measurements were considered. With spatially resolved observations, the BLUEDISK survey aims to go one step forward compared to previous studies.

The main science objective of the BLUEDISK survey is to search for accretion signatures and therefore to characterize the gas distribution and kinematics of H I-rich galaxies. The BLUEDISK survey is a multiwavelength campaign of 50 nearby galaxies with similar stellar masses, of which about half are H I-rich galaxies and half are H I-normal or 'control' galaxies. The ancillary data of that survey comprise UV data from *GALEX*, optical broad-band data and spectroscopy from the Sloan Digital Sky Survey (SDSS), William Herschel Telescope (WHT) spectroscopy (PI Brinchmann; Carton et al. 2015) at a resolution of ∼1.5 arcsec, and Westerbork Synthesis Radio Telescope (WSRT) H I 21-cm data (PI Kauffmann; Wang et al. 2013, 2014) at a resolution of ∼15 arcsec. H I observations have revealed that the discs of the H I-rich sample are more extended relative to the optical size and generally more clumpy than in the control sample (Wang et al. 2013). The H I gas is not kinematically disturbed, giving preference to rather continuous accretion. The excess H I is located in the outer parts of the disc (beyond R_{25}, defined as the radius of the g-band 25 mag arcsec^{-2} isophote) for half of the H I-rich galaxies and in the centre for the other half (Wang et al. 2014). In the outer parts, the H I surface density profiles of the H I-rich and control galaxies are similar though. Moreover, all galaxies display gas-phase metallicity drops, which are steeper for the H I-rich sample and occur at larger stellar radii for the control sample (Carton et al. 2015).

Observations of the cold, star-forming molecular gas are necessary to study the evolution of the star formation properties and disc growth in those galaxies. In this paper, we present CO observations with the IRAM-30m telescope of 26 galaxies from the BLUEDISK survey, listed in Table 1. The main goal is to investigate whether the H I-rich galaxies have different molecular gas properties than the control galaxies, and what the implications for the evolution of those galaxies are. To do this, we compare the amount and distribution of

atomic and molecular gas to the star formation rate (SFR) between the two samples, and we relate those quantities to galaxy morphology, metallicity, and stellar densities. We describe the observing strategy, data reduction, and further processing in Sections 3 and 4. Our results are presented in terms of integrated, resolved, and radial properties in Section 5, and discussed in Section 6. We summarize our findings in Section 7.

2 SAMPLE SELECTION

2.1 BLUEDISK sample

Selection of the BLUEDISK sample is described in detail in Wang et al. (2013). We summarize the main characteristics. Galaxies of the BLUEDISK survey are selected from the SDSS DR7 MPA/JHU catalogue and required to be massive ($10 < \log M_\star/M_\odot < 11$), nearby ($0.01 < z < 0.03$), northern (Dec. $> 30^\circ$) and extended enough on the sky to be resolved ($D_{25} > 50$ arcsec). The H I-rich sample consists of galaxies that are above the Fundamental Plane[1] defined by Catinella et al. (2013). The H I-rich galaxies have ∼3 times higher M(H I) than the median at the same $M_\star$. The control sample lies close to that plane, with galaxies closely matched to the H I-rich sample in stellar mass ($M_\star$), stellar surface density ($\mu_\star$), redshift and inclination, but with normal H I content.

2.2 CO follow-up

Due to sensitivity limitations, not all of the BLUEDISK galaxies could be observed with IRAM. We decided to target a sub-sample of 26 galaxies (Table 1), mapping the brightest ones with the HEterodyne Receiver Array (HERA) and observing with single pointings the others with the Eight Mixer Receiver (EMIR). The target selection was done by identifying the most H I-rich or highest SFR galaxies and their paired galaxies, while covering a range of parameters (M(H I), $M_\star$, SFR) close to that covered by the full BLUEDISK sample (Fig. 1). This is driven largely by observability considerations (reducing the number of receiver tunings/overheads while keeping a sufficiently large number of galaxies).

Of the 26 galaxies in our sub-sample, 15 belong to the H I-rich sample and 11 belong to the control sample. Two H I-rich galaxies (ID29 and ID31) are not isolated but multisource systems. We include them in the figures (1 and 2) as black symbols but exclude them from correlations and hence label them as excluded in Table 1. Note that ID41 was also labelled as excluded in Wang et al. (2013) because initially no H I data were taken for this galaxy. Since we have obtained new WSRT H I observations for this galaxy, we re-include it as a control galaxy.

3 OBSERVATIONS

3.1 HERA observations of CO(2–1)

3.1.1 Observing details

We mapped 15 BLUEDISK galaxies in the ^{12}CO(2–1) line at 230.54 GHz with the HERA instrument. The spatial resolution achieved with HERA, which has a half power beam width of 11 arcsec, is ∼6.5 kpc at the median distance of our sample (120 Mpc). HERA is a heterodyne receiver consisting of 3 × 3 pixels separated by 24 arcsec, with two orthogonal polarizations. Observations were performed in the on-the-fly mapping mode to map an area of about 1.2 arcmin × 1.2 arcmin, slightly larger than the optical disc size of our galaxies. To make maps as uniform as possible and fill the gaps between the detectors, we used the oversampling observing mode[2] and performed up and down scans separated by 12 arcsec along two alternated perpendicular directions oriented 45° from the major axis. The pattern is repeated as many times as required to achieve the desired rms. We used the backend WILMA, which covers a total bandwidth of 8 GHz per polarization (∼11 000 km s^{-1} at the observed frequency 225 GHz), with velocity resolution 2.6 km s^{-1}. Observations were carried out between 2012 October and 2014 March, under good winter conditions (mean zenith opacity of 0.08 at 225 GHz), as part of the programs 073-12 (PI Bigiel; 35 h) and 205-13 (PI Cormier; 50 h). The average system temperature was 340 K. The observing details are given in Table 2.

Table 2. Details of the IRAM 30-m observations.

Galaxy ID	Observing dates	Noise (mK)
	HERA observations	
ID1	2012 December 1, 2014 March 11	3.9
ID2	2012 December 2	6.1
ID3	2014 March 8, 9	4.5
ID4	2012 December 3, 2014 March 10, 11	3.6
ID5	2012 October 15	10
ID6	2012 December 1	8.1
ID8	2012 December 2	4.9
ID9	2014 January 14, March 7, 8	3.1
ID10	2012 December 2	4.5
ID11	2012 December 3	6.5
ID14	2012 December 3	6.6
ID15	2012 December 2	5.7
ID16	2014 March 8	4.0
ID17	2012 December 2, 2014 March 8	2.6
ID20	2012 December 2, 2014 March 11	4.1
	EMIR observations	
ID27	2014 March 9, 10	2.3, 3.0
ID29	2014 February 8	1.4, 2.6
ID31	2014 March 9	2.7, 3.9
ID33	2014 February 8	1.4, 2.2
ID35	2014 January 12	2.3, 3.3
ID37	2014 January 12	1.8, 3.0
ID40	2014 March 9	2.7, 3.5
ID41	2014 January 10	1.6, 3.1
ID43	2014 January 12	1.9, 3.1
ID44	2014 January 12	2.5, 3.8
ID47	2014 March 9, 10	1.6, 2.0

Notes. The noise level (in units of T_{mb}) for the HERA observations is taken as the median value of the error maps (see Section 3.1.3). For the EMIR observations, the noise level in both the CO(1–0) and CO(2–1) spectra are indicated (left and right values, respectively), at a spectral resolution of 15.6 km s^{-1}.

3.1.2 Data reduction of the spectral cubes

The data reduction was performed using the Continuum and Line Analysis Single-dish Software (CLASS), which is part of the GILDAS

[1] $\log(\mathrm{M(H\,I)}/M_\star) + 0.234 \times \log(\mu_\star) + 0.342 \times (NUV - r) - 2.329 = 0$

[2] http://www.iram.es/IRAMES/otherDocuments/manuals/HERA_manual_v20.pdf

package.[3] The steps are as follows, and executed for each galaxy. We first read the data in, selected the part of the spectra around the expected line centre (about $\pm 600\,\mathrm{km\,s^{-1}}$), and ignored bad spectra (strange baseline, fringes) as well as data from the unstable pixels 4 and, for the 2014 observations, 9 of the second receiver. The data were shifted to rest frame using the velocity from optical data converted to the radio definition, and put in units of main beam temperature using a beam efficiency value extrapolated from the measured value of 0.58 at 230 GHz[4] to our observed frequencies with the Ruze's equation and a forward efficiency of 0.94. We then applied a baseline correction of polynomial degree 0 (masking the inner $\pm 200\,\mathrm{km\,s^{-1}}$ where the line is expected) and excluded spectra with overall noise above three times the theoretical noise. Spectral cubes were produced by projecting the remaining spectra on a grid of pixel size 2 arcsec, with final spatial resolution 13.5 arcsec (convolved with a Gaussian kernel) and spectral resolution $15.6\,\mathrm{km\,s^{-1}}$. We clipped the very edges of the map where the noise increased due to smaller number of scans from our mapping strategy. For this, we clipped pixels with time weights below a value of 0.03 typically.

To further improve the baseline correction, we defined spectral windows to mask the CO line based on the H I data. H I moment maps from Wang et al. (2013) with robust weighting of 6 and tapering of 30 arcsec, which optimize the sensitivity, were used. Our first assumption was that CO emission is expected inside the H I envelope, hence our windows were defined at positions where H I is detected at $\geq 5\sigma$ level in the moment zero maps. We used the H I first- and second-order moment maps to determine the centre and width of the CO windows. Then, we iterated the process and adapted the windows by hand (where the CO line is clearly detected) to ensure that our windows are as narrow as possible while encompassing all the CO emission. Since the CO line profiles are observed to be wider at the galaxy centre than in the disc, the windows were made wider at the centre and around the minor axis and linearly decreasing in size going to larger radii. Beyond 0.7 R_{25} typically, where CO is not clearly detected, we kept the size of the window fixed to $\sim$0.7 times the window size at the galaxy centre.

Once our windows were finalized, we masked all velocity channels inside each window and fit a polynomial of degree 1 to correct for the baseline.

3.1.3 *Intensity and error maps*

We created moment maps after masking all channels outside of the windows. At the mean distance of our sample, we probe linear scales of 6.5 kpc. The line widths are large, from $80\,\mathrm{km\,s^{-1}}$ to $240\,\mathrm{km\,s^{-1}}$ at the centre of the disc, and the CO profiles are not Gaussian. Hence, we prefer to use moment maps rather than perform a line fit. The intensity maps and averaged spectra within a circular aperture of diameter 22 arcsec on the galaxy centres are shown in Appendix. Linewidths are smallest for ID1, ID5, and ID10, and larger than $200\,\mathrm{km\,s^{-1}}$ for the other galaxies.

We also generated maps reflecting the statistical error on the intensities. For each spectrum, the error is calculated as the standard deviation on the baseline (channels outside of the window), multiplied by the channel width times the square root of the number of channels inside the window. This is the error per window and it is independent of the channel size.

To verify the accuracy of the described method and that we are not biasing the results when including manual steps, we also produced moment maps for which the windows were defined: (1) centre from H I moment 1 maps and width where H I is emitting above a 3σ level (i.e. without further refinement); and (2) centre from H I moment 1 maps and a fixed width. The three methods generally agree within the errors, but the manual method tends to produce better signal-to-noise maps. With a fixed window, some of the CO emission is sometimes missed, and based on the H I only, the windows often include noisy channels which degrade the results.

3.2 EMIR observations of CO(1–0) and CO(2–1)

3.2.1 *Observing details*

We used the EMIR instrument to simultaneously observe the ^{12}CO(1–0) and ^{12}CO(2–1) lines in 11 BLUEDISK galaxies. The rest frequencies are 115.27 and 230.54 GHz, and the half power beam widths are 22 arcsec ($\sim$13 kpc) and 11 arcsec ($\sim$6.5 kpc), respectively. We made pointed observations in ONOFF wobbler switching mode with a wobbler throw between 55 and 120 arcsec (80 arcsec in general) depending on the source. The WILMA backend was connected. Observations were carried out between 2014 January and March, under good winter conditions (mean zenith opacity of 0.16 at 225 GHz), as part of the program 205-13. The average system temperature was 340 K.

3.2.2 *Data reduction*

The data were reduced with CLASS. For each galaxy, we extracted spectra in a bandwidth of 1 GHz around the observed line frequency. The spectra were shifted to rest frame using the radial velocity, and put in units of main beam temperature using beam efficiency values extrapolated from the measured values of 0.78 at 115 GHz and 0.58 at 230 GHz to our observed frequencies with the Ruze's equation and forward efficiencies of 0.92 and 0.94, respectively. The spectra were then averaged and rebinned to a spectral resolution of $15.6\,\mathrm{km\,s^{-1}}$. A baseline correction of polynomial degree 3 was applied. We measured the rms of the data as the standard deviation on the continuum, i.e. outside of a $\pm 200\,\mathrm{km\,s^{-1}}$ window around the expected line centre (see Table 2).

The spectra are shown in Fig. A2. Several spectra have double-peaked profiles, others have asymmetric profiles, especially ID 31 which is an interacting system. The lines are detected in all galaxies, except CO(2–1) in ID33 and a marginal detection in ID41. The CO intensities are reported in Table 3. They were derived by integrating the signal inside a window of size $\sim 250\,\mathrm{km\,s^{-1}}$ depending on the source.

3.3 Sources of uncertainty

Besides statistical errors, there are other systematic sources of uncertainty to be aware of. IRAM flux calibration uncertainties are on the order of 10 per cent and pointing accuracy is about 2 arcsec. Uncertainties on the quantities listed in Table 3 only include statistical errors.

3.4 WSRT observations of H I 21-cm

To complement the H I 21-cm data set of the BLUEDISK survey published in Wang et al. (2013), we observed H I in the galaxy ID41 with the WSRT. ID41 was not observed in the initial survey due to

[3] http://www.iram.fr/IRAMFR/GILDAS
[4] http://www.iram.es/IRAMES/mainWiki/Iram30mEfficiencies

Table 3. CO intensities, gas masses, and star formation rates.

Galaxy ID	$I_{CO(1-0)}$ (K km s^{-1})	$I_{CO(2-1)}$ (K km s^{-1})	$M_{H_2,22}$ (log M$_\odot$)	$M_{H_2,total}$ (log M$_\odot$)	$M_{H\,I,22}$ (log M$_\odot$)	$M_{H\,I,total}$ (log M$_\odot$)	SFR$_{22}$ (M$_\odot$ yr^{-1})	SFR$_{total}$ (M$_\odot$ yr^{-1})
BLUEDISK galaxies observed with HERA								
ID1	–	{1.37(0.20)}	8.95(7.84)	9.27(8.73)	8.90(7.71)	10.10(8.44)	1.37(0.01)	3.16(0.01)
ID2	–	{0.58(0.33)}	8.39(8.06)	8.66*	9.13(7.67)	9.95(8.25)	0.22(0.01)	0.65(0.01)
ID3	–	{1.77(0.35)}	9.14(8.31)	9.35(7.98)	9.13(7.82)	9.91(8.36)	1.41(0.01)	3.39(0.04)
ID4	–	{2.70(0.22)}	9.20(7.75)	9.50(8.62)	9.27(7.77)	10.27(8.52)	1.39(0.01)	4.74(0.03)
ID5	–	{3.57(0.60)}	9.29(8.42)	9.63(9.09)	8.87(7.65)	10.21(8.58)	2.42(0.01)	5.62(0.01)
ID6	–	{2.00(0.60)}	9.06(8.52)	9.44*	8.83(7.67)	10.33(8.51)	0.36(0.01)	0.88(0.06)
ID8	–	{1.89(0.31)}	9.14(8.49)	9.40*	8.88(7.74)	10.21(8.57)	0.45(0.01)	1.97(0.01)
ID9	–	{2.97(0.20)}	9.31(8.07)	9.52(8.50)	9.20(7.89)	9.93(8.33)	2.03(0.01)	5.38(0.01)
ID10	–	{3.84(0.24)}	9.49(8.37)	9.76(8.77)	9.01(7.83)	10.05(8.46)	3.18(0.01)	8.31(0.02)
ID11	–	{3.11(0.41)}	9.20(8.23)	9.49(8.89)	8.88(7.87)	9.73(8.11)	0.84(0.01)	2.52(0.01)
ID14	–	{1.53(0.50)}	8.93(8.50)	9.24*	8.99(7.65)	10.15(8.47)	0.49(0.01)	1.84(0.01)
ID15	–	{3.06(0.42)}	9.08(7.96)	9.50(9.06)	8.66(7.50)	10.40(8.58)	0.74(0.01)	3.83(0.04)
ID16	–	{2.12(0.23)}	9.13(7.82)	9.30(8.51)	9.22(7.93)	10.02(8.50)	2.32(0.01)	5.50(0.01)
ID17	–	{1.01(0.16)}	8.83(7.89)	9.05(8.45)	8.84(7.98)	10.23(8.82)	0.78(0.01)	2.05(0.01)
ID20	–	{1.98(0.24)}	9.12(8.35)	9.33(8.67)	9.21(7.76)	10.22(8.50)	1.15(0.01)	3.66(0.02)
BLUEDISK galaxies observed with EMIR								
ID27	2.57(0.18)	1.90(0.23)	9.36(8.21)	9.48*	8.87(7.70)	9.36(7.96)	1.05(0.01)	2.25(0.01)
ID29	2.43(0.14)	3.48(0.27)	9.23(7.98)	9.48*	9.17(7.91)	10.23(8.65)	0.58(0.01)	1.62(0.03)
ID31	4.94(0.20)	7.65[a](0.30)	9.55(8.17)	9.71*	9.21(7.74)	9.89(8.39)	2.63(0.01)	6.60(0.01)
ID33	0.94(0.15)	0.25[b](0.25)	8.85(8.05)	9.09*	8.59(7.57)	9.33(7.68)	0.27(0.01)	0.64(0.03)
ID35	2.95(0.23)	3.15(0.33)	9.26(8.16)	9.50*	8.96(7.61)	9.92(8.37)	0.46(0.01)	1.00(0.01)
ID37	2.94(0.16)	3.06(0.26)	9.32(8.07)	9.56*	8.99(7.74)	9.72(8.10)	0.67(0.01)	1.85(0.01)
ID40	3.13(0.23)	3.78(0.31)	9.39(8.26)	9.55*	8.81(7.66)	9.69(8.31)	0.71(0.01)	1.57(0.03)
ID41	1.51(0.16)	1.43(0.31)	9.15(8.17)	9.37*	8.59(7.69)	9.43(8.01)	0.43(0.01)	1.25(0.01)
ID43	2.53(0.20)	3.36(0.32)	9.29(8.18)	9.45*	8.77(7.69)	9.61(8.18)	0.60(0.01)	1.35(0.01)
ID44	2.56(0.23)	4.14(0.34)	9.33(8.28)	9.55*	8.77(7.71)	9.40(7.75)	1.42(0.01)	3.41(0.02)
ID47	1.66(0.15)	1.76(0.14)	9.00(7.97)	9.24*	8.65(7.62)	10.01(8.48)	0.25(0.01)	1.02(0.01)

Notes. The EMIR beam sizes are 22 and 11 arcsec for CO(1–0) and CO(2–1), respectively. EMIR intensities are given per beam. HERA intensities are averages within a circle of diameter ∼22 arcsec positioned on the galaxy centre. Uncertainties are indicated in parenthesis and correspond to statistical errors. Total masses are measured out to $R = 0.7 \times R_{25}$ for $M_{H_2,total}$ and $R \simeq 3 \times R_{25}$ for SFR$_{total}$ and $M_{HI,total}$. [a]the CO(2–1) line shape is more asymmetric than that of CO(1–0). We may be missing extended emission due to the different beam sizes. [b]1σ limit on the CO(2–1) intensity. *Mass extrapolated from the central measurement (see Section 4.4).

time constraints. The data were obtained in 2014 February, with an on-source integration time of 13 h, as part of the program R14A028 (PI Bigiel). The reduction steps are identical to those performed in Wang et al. (2013) and the H I masses are reported in Table 3. The beam size is 16 × 20 arcsec^2, the velocity resolution is 12.4 kms and the noise level is 0.33 Jy beam^{-1}.

4 ANALYSIS

In this study, we work with integrated results for each galaxy and radial profiles for galaxies mapped in CO. We describe how those measurements are made in the following.

4.1 Surface density maps

To compare interstellar medium tracers to star formation properties, we create surface density maps of H_2, H I, and SFR (denoted Σ_{H_2}, $\Sigma_{H\,I}$, and Σ_{SFR}). The CO(2–1) intensities are converted to H_2 surface densities assuming an intensity ratio of CO(2–1)/CO(1–0) of 0.8 and a Galactic conversion factor $\alpha_{CO} = 4.38$ M$_\odot$ pc^{-2} (K km s^{-1})$^{-1}$, which includes helium, both appropriate for Milky Way-type galaxies (e.g. Leroy et al. 2013). We compare the assumed CO line ratio to that measured with EMIR in Section 4.4.2 and we discuss effects of using a metallicity-dependent conversion factor in Section 5.1. The H I products are taken from Wang et al. (2013) and we refer to that paper for information on the data acquisition and processing of the BLUEDISK galaxies. We use the same version of the H I data as in their analysis, i.e. with robust weighting of 0.4 and no tapering, which is the best compromise between sensitivity and resolution. The SFR is measured from a combination of archival *Wide-field Infrared Survey Explorer* (*WISE*) 22 μm [5] (Wright et al. 2010) and *GALEX* FUV[6] (Martin et al. 2005) data. We first removed a background using areas of the maps where there is no signal, convolved the maps from their native resolution (12 arcsec for *WISE* 22 μm, 4.2 arcsec for *GALEX* FUV) to a resolution of 13 arcsec with a Gaussian kernel, and converted the *WISE* fluxes to *Spitzer*/MIPS 24 μm fluxes using a conversion factor of 0.86 (based on the Chary & Elbaz 2001 templates and respective response curves). The data sets are then combined using the formula from Leroy et al. (2008): $\Sigma_{SFR} = 0.081 \times I_{UV} + 0.0032 \times I_{24}$. In addition, we compare the gas masses and SFR to metallicity measurements. Optical spectroscopy was obtained with the WHT and converted to oxygen abundance using the models of Charlot & Longhetti (2001) (see Carton et al. 2015, for details). Observations consisted of a slit passing through the centre of each disc and aligned with the rotation axis of the galaxy. Note that ID6, ID11, ID15 and

[5] http://wise2.ipac.caltech.edu/docs/release/allsky/
[6] http://galex.stsci.edu/GR6/

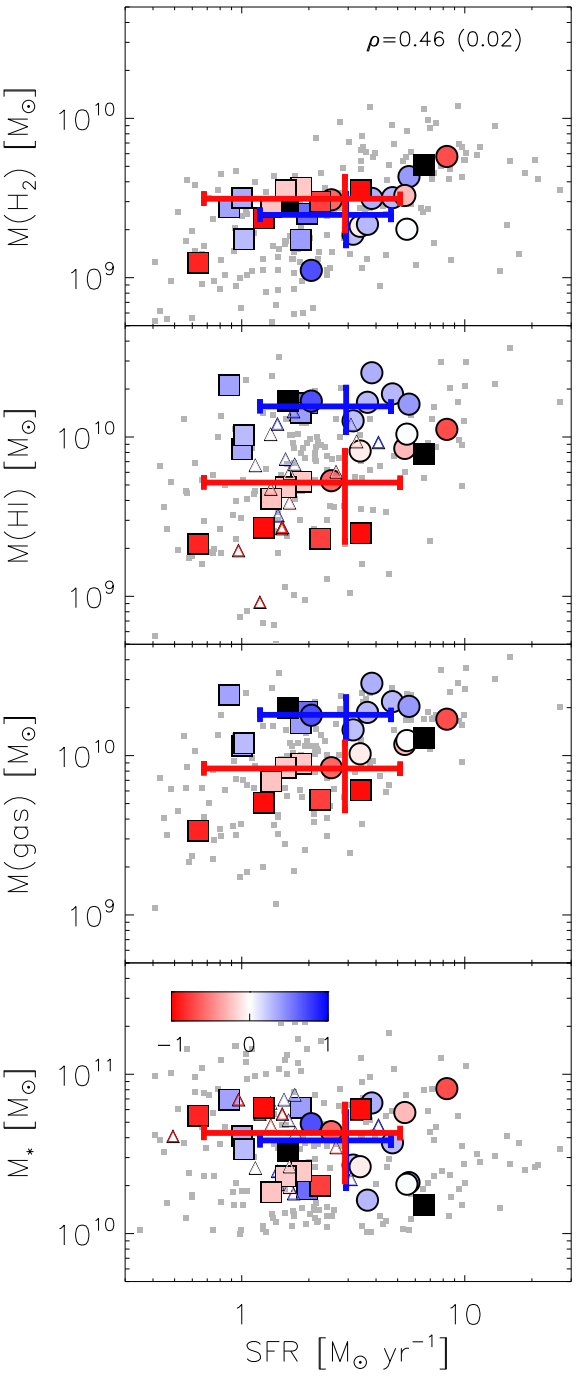

Figure 1. Comparison of stellar and gas masses as a function of SFR. Circles are galaxies with measured CO masses (HERA sample) and squares are galaxies with CO central measurements extrapolated to total masses (EMIR sample and ID2, 6, 8, 14); see Section 4.4.1 for details. Open triangles are galaxies not observed in CO. Colour-coding is based on the distance from the plane in fig. 3 of Catinella et al. (2013). H I-rich galaxies are above the plane, control galaxies are below that plane, and excluded galaxies are in black. The mean and standard deviation of each quantity are overplotted as crosses for the H I-rich and control samples. The background grey data points are CO-detected galaxies from the COLD GASS 3rd data release (Saintonge et al. 2011b).

ID17 do not have metallicity measurements at their centre because of signatures of non-star formation activity [active galactic nuclei (AGN)/low-ionization nuclear emission-line region] in their optical spectra (Carton et al. 2015). However, the *WISE* colours based on bands 1, 2 and 3 at shorter wavelengths indicate that our galaxies do not fall in the AGN wedge but have colours compatible with those of star-forming galaxies (Wright et al. 2010; Mateos et al. 2012). Therefore, we do not expect the derived SFR to be significantly contaminated by AGN activity.

4.2 Structure in the CO maps

At a working resolution of ∼13 arcsec, we detect CO emission (above 3σ) in the BLUEDISK galaxies mapped with HERA in roughly four independent beams. As a consequence, we cannot identify clear sub-structure, but we do see extended CO emission (see the maps in Appendix). CO peaks at the optical centre of the galaxies and is usually elongated along the major axis. The signal-to-noise ratio is low for ID2, ID6, ID8, and ID14. Their CO intensity maps appear patchy because CO is detected only in the brightest peaks. We present their profiles but we exclude them from any quantitative radial analysis. CO and H I emission follow each other well globally. The CO and H I peaks are noticeably offset (by at least 10 arcsec) in ID5, ID6, ID8, ID11, ID15, and ID17. This is because the H I emission is less centrally concentrated, or, in the cases of ID15 and ID17, more clumpy. Visual inspection of the CO intensity maps indicates that features appearing outside of the optical discs are most likely noise rather than emission from a companion galaxy. We note that for individual galaxies:

(i) *ID1:* the knots N and S of the central emission blob are real and coincide with the spiral arms of the galaxy.
(ii) *ID3:* the two stripes in the NE direction are noise.
(iii) *ID11:* the extensions of the main peak to the N and E are in agreement with the asymmetric H I distribution. There seems to be a companion in the optical and H I deficit to the NE.
(iv) *ID15:* the emission in the SE is bright and may be connected to the spiral arm.

4.3 Radial profiles

To analyse the radial behaviour of the different tracers, we produce surface density profiles as a function of radius, with step size 1/2 of the spatial resolution of the CO data (i.e. 6.5 arcsec) and out to a radius of 1.5 R_{25}. We caution that this sampling applies to the major axis, but for highly inclined galaxies, the minor axis remains largely unresolved. At a given radius, we consider the average surface density within a tilted ring of width ±0.5 times the chosen step size. The assumed inclinations and position angles are given in Table 1. Those are measured from SDSS *r*-band data. Error bars on the profile measurements are also taken as the average within each ring in our error maps. All profiles are corrected for inclination. The radial profiles of Σ_{H_I}, Σ_{H_2}, Σ_{SFR}, metallicity, and their associated errors are shown in Fig. 3 and discussed in Section 5.2.

4.4 Integrated results

4.4.1 Quantities: total and within 22 arcsec

Most of the control galaxies have CO(1–0) observed only in their centre (EMIR beam size of 22 arcsec at 115.3 GHz) and we have full coverage of the molecular emission mainly for the H I-rich galaxies

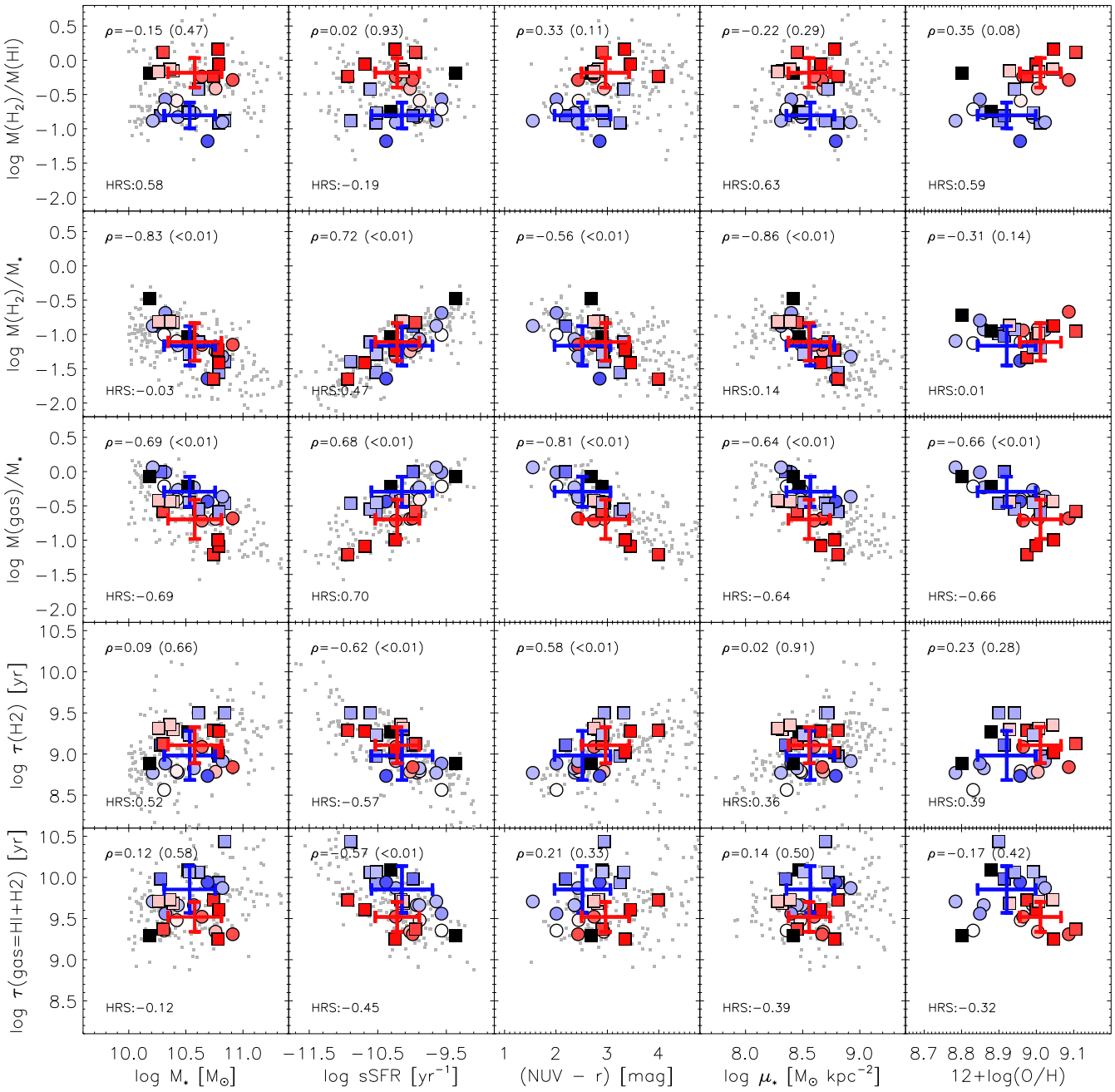

Figure 2. Scaling relations for the BLUEDISK galaxies. We show the molecular fraction, $M(H_2)/M(H\,I)$, the molecular and atomic to stellar mass ratios, $M(H_2)/M_\star$ and $M(H\,I)/M_\star$, the molecular gas depletion time, τ_{H2}, and total gas depletion time, $\tau_{gas=H\,I+H_2}$, as a function of stellar mass, specific SFR, sSFR, colour, $NUV - r$, stellar mass surface density, $\mu_\star$, and metallicity, for total measurements of the BLUEDISK galaxies. Same colour-coding as in Fig. 1. The mean and standard deviation of each quantity are overplotted as crosses for the H I-rich and control samples. We also indicate Pearson correlation coefficients of the BLUEDISK galaxies as well as coefficients of the HRS galaxies for comparison (Boselli et al. 2014b). The background grey data points are CO-detected galaxies from the COLD GASS 3rd data release (Saintonge et al. 2011b).

which molecular gas discs were mapped with HERA. Therefore, for all galaxies, we compile measurements of molecular gas mass, atomic gas mass, and SFR inside an aperture of diameter 22 arcsec as well as total measurements. For total measurements, we perform aperture photometry (with weights of 1 inside the aperture and weights of 0 outside the aperture) on the CO (if available), H I and SFR maps. Total quantities are derived out to a radius of $0.7 \times R_{25}$ for the molecular gas and out to $3 \times R_{25}$ for the atomic gas and SFR. When doing aperture photometry, the integrated errors correspond to the quadratic sum of the errors multiplied by the square root of the oversampling factor of the beam.

For the galaxies that have CO(1–0) observed only in their centre (EMIR sample) or CO(2–1) mapped but detected only in their centre (ID2, ID6, ID8, and ID14), we estimate their total molecular gas mass by extrapolation of their central measurements. We assume that CO is distributed in an exponential disc of scalelength $0.2 \times R_{25}$

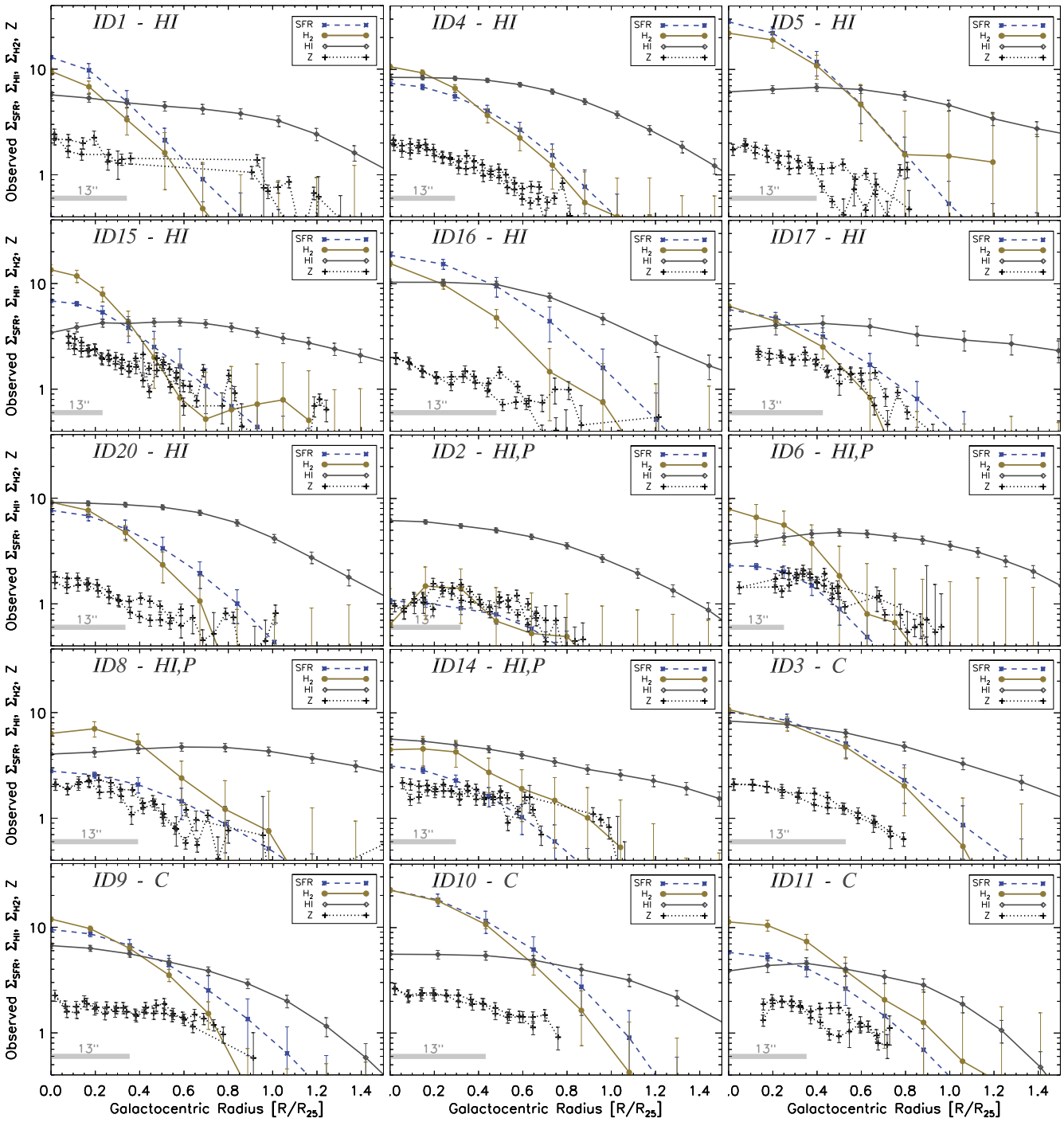

Figure 3. Surface density profiles, corrected for inclination, of Σ_{H_2}, $\Sigma_{H\,I}$ (in units of $M_\odot$ pc^{-2}), and Σ_{SFR} (in units of 10^{-3} $M_\odot$ yr^{-1} kpc^{-2}) as a function of radius (normalized to R_{25}) for each galaxy mapped with IRAM/HERA. Horizontal grey bars indicate the angular resolution. The dotted lines are metallicity profiles from Carton et al. (2015), with two values for each radius because the slit of the telescope passes through the centre, and normalized to the solar metallicity ($Z_\odot$ =12 + log (O/H) = 8.82). Profiles are shown in the following order: H I-rich discs of good quality (HI), H I-rich discs of poor quality (HI,P), and control discs (C). Average behaviours are shown in Fig. 5.

(e.g. Leroy et al. 2008; Lisenfeld et al. 2011) and we employ the 2D prescription of Boselli, Cortese & Boquien (2014a) since none of our discs are edge-on (their equations 9 and 10). This extrapolation corresponds to a correction factor of the central mass to the total mass of a factor of ∼2 (see Table 3). Testing this method on the galaxies that were actually mapped, we find that the molecular gas masses measured inside a radius of 0.7 × R_{25} and those extrapolated from their central mass agree within 20 per cent. This gives confidence in the methods. We also tried to use individual scalelengths of the stellar disc from the stellar surface density maps of Carton et al. (2015), instead of the canonical value of 0.2, but for the mapped galaxies, the scatter between the measured total mass and the mass extrapolated from the centre is not improved. For consistency, we prefer to use the fixed value of 0.2.

4.4.2 The CO(2–1)/CO(1–0) intensity ratio

For the EMIR galaxies, we have obtained with central pointings both CO(1–0) and CO(2–1) in different beam sizes (22 and 11 arcsec, respectively). The intensity ratio at face value (assuming uniform distribution) varies between 0.65 and 1.6, which is globally higher than the standard value of ∼0.8 observed in nearby disc galaxies (e.g. Leroy et al. 2009). In the case of point-like emission, the ratios have to be corrected for the difference in beam solid angles and thus multiplied by 1/4. Note that both scenarios are likely not good assumptions for the distribution of CO emission in the inner parts of galaxies which often decreases exponentially with radius.

Given the size of the optical radii of our galaxies, we expect CO emission to be marginally extended compared to the EMIR beam. In order to compare the intensities of the two CO transitions, a more realistic approach would be to correct for the aperture difference assuming a radial decline of the CO emission. Here, we use the HERA data to simulate what would be the CO(2–1) mean surface brightness as if observed by a single pointing. We employed two different methods: circular aperture photometry, and multiplying our map with a Gaussian kernel. We find the two methods to be equivalent within ∼5–15 per cent for full widths at half maximum of 22 and 11 arcsec, respectively. Therefore, we prefer to use the aperture photometry method for simplicity. The CO(2–1) mean surface brightness within a diameter of 22 arcsec about the centre is 0.60–0.95 times lower than the mean surface brightness within a diameter of 11 arcsec. Hence, for the EMIR data, we multiply the observed CO(2–1) intensity (for which the beam size is 11 arcsec) by a factor of 0.75 to estimate what would be the CO(2–1) intensity in 22 arcsec, and we compare this estimate to the observed CO(1–0) intensity (for which the beam size is 22 arcsec). Doing so, we find CO intensity ratios between 0.5 and 1.2 in the EMIR galaxies, with a median value of 0.8. If conditions in the CO-emitting clouds are similar in the H I-rich and control galaxies, this validates our choice of a CO(2–1)/CO(1–0) intensity ratio of 0.8 used for the discs mapped with HERA where we have no CO(1–0) data.

5 RESULTS

5.1 Comparison to the surveys COLD GASS and HRS

We compare total gas quantities with general galaxy parameters for the BLUEDISK galaxies and contrast our findings with the results from COLD GASS (Saintonge et al. 2011a,b) and HRS (Boselli et al. 2014a,b) in Figs 1 and 2. Trends between variables (in logarithmic scale) are quantified with the Pearson correlation coefficient and their significance are indicated in parenthesis. COLD GASS studied a sample of 215 CO-detected galaxies at redshifts $0.025 < z < 0.05$ and stellar masses $10.0 < \log M_\star/\mathrm{M}_\odot < 11.5$, while the HRS sample consists of 143 CO-detected galaxies at $z < 0.005$ and $9.0 < \log M_\star/\mathrm{M}_\odot < 11.0$.

Fig. 1 shows the mass of stars, atomic, molecular and total gas (atomic + molecular) as a function of SFR for the BLUEDISK galaxies. We find that the H I-rich galaxies span the same range of SFR and stellar masses as the control galaxies. They clearly have more H I, by a factor of ∼4 on average, but they have similar H_2 masses. Overall, the SFR is not correlated with the stellar mass, nor with the H I mass, but is correlated with the H_2 mass (Pearson correlation coefficient $\rho \simeq 0.46$). Our BLUEDISK galaxies fall within the range of parameters covered by the COLD GASS sample, with the H I-rich galaxies being on the upper end of the H I and total gas mass distributions. Comparing the ranges of parameters covered by the entire BLUEDISK sample, the sub-sample of galaxies that we observed in CO seems representative of the whole BLUEDISK sample. The galaxies mapped with HERA are amongst the most H I-rich and actively star-forming characteristics to keep in mind for the interpretation of our resolved analysis in the context of galaxy evolution.

Fig. 2 shows the molecular fraction, $M(H_2)/M(\mathrm{H\,I})$, the molecular and total gas mass to stellar mass ratios, $M(H_2)/M_\star$ and M(gas)/$M_\star$, the molecular gas depletion time, τ_{H2}, and the total gas depletion time, $\tau_{\mathrm{gas=H\,I+H_2}}$, as a function of stellar mass, specific star formation rate, sSFR, colour, $NUV - r$, stellar mass surface density, $\mu_\star$, and average metallicity. The depletion time is defined as the mass of gas divided by the SFR. The average values of $M(H_2)/M_\star$ and M(gas)/$M_\star$ are ∼0.1 and 0.4, respectively, with the H I-rich galaxies having ∼3 times larger total gas masses than the control galaxies. The mean value of $M(H_2)/M(\mathrm{H\,I})$ is ∼40 per cent in both the BLUEDISK and COLD GASS samples (Saintonge et al. 2011a). However, we find that the H I-rich galaxies have systematically four times lower $M(H_2)/M(\mathrm{H\,I})$ ratios compared to the control galaxies, independently of global galaxy parameters. Our molecular gas fractions are not as well correlated with galaxy parameters as for the HRS survey. This may be a sample effect as the H I-rich galaxies were selected specifically for their large H I masses. The trend of increasing molecular fraction with metallicity that we observe in the BLUEDISK could point to an underestimation of the molecular gas mass from CO in the lower metallicity galaxies (e.g. Bolatto, Wolfire & Leroy 2013; Cormier et al. 2014). The mean metallicities of the H I-rich and control samples are higher than solar and differ only by 0.1 dex though. Correcting masses with the metallicity-dependent prescription of X_{CO} from Bolatto et al. (2013) (their equation 31) would increase global H_2 masses by up to 10 per cent in the H I-rich galaxies. Hence, the offset in the $M(H_2)/M(\mathrm{H\,I})$ values is unlikely to be due to X_{CO} conversion factor effects only, given the small range of metallicities spanned by our galaxies.

Generally, the trends that appear are similar to those found by Boselli et al. (2014b). The strongest correlations are found for $M(H_2)/M_\star$, decreasing with $M_\star$ and $\mu_\star$ and increasing with sSFR; and for M(gas)/$M_\star$, decreasing with $M_\star$, $\mu_\star$, $NUV - r$, and metallicity and increasing with sSFR. Interestingly, the H I-rich and control galaxies seem to follow parallel trends in some of those plots. Our correlations with $M(H_2)/M_\star$ are more significant than those found for the HRS galaxies and closer to what Saintonge et al. (2011a) found. Again, this is probably a selection effect as our galaxies do not span a range of galaxy properties as wide as the HRS survey. We also find that the molecular depletion time, τ_{H2}, is not constant. It varies between 0.4 and 4 Gyr, which is compatible with previous studies in the stellar mass range probed. It is marginally higher in the control galaxies than in the H I-rich galaxies, by a factor of 1.4 on average, because they are slightly more molecular-rich (Fig. 1). Yet, total gas depletion times are clearly higher in the H I-rich galaxies since H I dominates their gas budget.

To summarize, the main characteristics of the H I-rich galaxies in comparison to the control galaxies are: larger H I masses, bluer colours and lower average metallicities, for similar stellar masses, molecular masses and SFR. Within the accuracy of our methods, the bluer colours in our galaxies seem to be related to a separation of the H I-rich/control samples in metallicity rather than a separation in SFR. The low H_2/H I ratios indicate that no H_2 formation out of accreted H I gas has occurred yet.

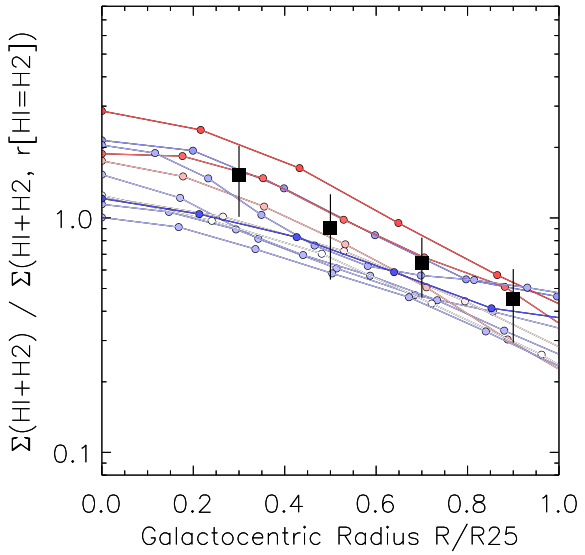

Figure 4. Total gas profiles (H I + H_2) of the 11 BLUEDISK galaxies with reliable profiles, normalized to the surface density at the transition radius (where $\Sigma_{H\,I} = \Sigma_{H_2}$). Same colour-coding as in Fig. 1. The mean values found by Bigiel & Blitz (2012) in nearby, late-type discs are overplotted as black squares.

We refer the reader to Section 6 for a discussion of those results. In the remainder of this section, we focus the analysis on the BLUEDISK galaxies mapped with HERA for which we have spatial information on the physical quantities.

5.2 Radial behaviours

Our goal in this section is to analyse radial behaviours, specifically of the gas and SFR distributions, as a function of distance to the disc centre.

Fig. 3 shows radial profiles for each disc. Σ_{H_2} and Σ_{SFR} generally behave similarly with radius and decline more rapidly than $\Sigma_{H\,I}$, as observed in the nearby spiral galaxies of HERACLES (Bigiel et al. 2008). Σ_{H_2} is particularly elevated compared to Σ_{SFR} in the centre of ID11 and ID15. Focusing on the centres of the galaxies, only ID2 seems H I-dominated, ID5, ID10, ID11, and ID15 are clearly H_2-dominated, while the other discs have similar values (within a factor of 2) of Σ_{H_2} and $\Sigma_{H\,I}$. The transition between the H_2-dominated and H I-dominated regimes always occurs at radii $R < 0.7\,R_{25}$, where $\Sigma_{gas} > 10\,M_\odot\,pc^{-2}$. Those are roughly compatible with transition radii of nearby, late-type discs ($\sim 0.5 \times R_{25}$; Bigiel & Blitz 2012). The transition radius in the BLUEDISK galaxies is smallest for the very H I-rich galaxies and largest for the most active galaxy (ID10). Metallicity profiles show fluctuations on small scales. However, the limited spatial resolution of the gas data precludes us from measuring fluctuations on those scales.

Following Bigiel & Blitz (2012), we investigate whether the BLUEDISK galaxies have total gas profiles similar to the average *universal* profile of well-resolved late-type nearby disc galaxies. Exponential fits to each profile of Fig. 4 in the radius range 0.2–1.0 $\times$ R_{25} give a median scalelength of 0.58 with dispersion 0.13. This compares to the scalelength of 0.61 in the nearby discs studied by Bigiel & Blitz (2012), although the scatter in the slopes of our profiles is quite large. Wang et al. (2014) normalized the x-axis to R1 instead of R_{25}, where R1 is the radius where the H I column density reaches 1 $M_\odot\,pc^{-2}$. Doing so does not seem to reduce the scatter in our data. Several H I-rich galaxies have shallower total gas profiles and lie below the median relation of Bigiel & Blitz (2012) because of their flatter H I profiles and smaller transition radii. A universality in the profiles of the outer H I disc has also been highlighted by Wang et al. (2014, 2016) to explain the H I mass–size relation of galaxies. However, this profile universality may be weaker when considering the total gas for the BLUEDISK galaxies as they show a wider range of total gas profiles at $R < R_{25}$.

Fig. 5 shows the molecular surface density, Σ_{H_2}, the molecular fraction, $\Sigma_{H_2}/\Sigma_{H\,I}$, the metallicity, and the depletion times, $\Sigma_{H_2}/\Sigma_{SFR}$, $\Sigma_{H\,I}/\Sigma_{SFR}$, and $\Sigma_{gas}/\Sigma_{SFR}$, as a function of galactocentric radius. At a given radius, the dynamic range of those quantities is about a factor of 2 to 3 for the normalized molecular surface density and metallicity, and a factor of 5 for the depletion times and molecular fraction. Inspecting averages over the sample (thick black lines), the metallicity decreases by a factor of $\sim$3 and the molecular fraction by a factor of $\sim$8 out to $R \simeq 0.7 \times R_{25}$. The latter trend is less dramatic than the decrease of more than an order of magnitude observed in nearby spirals (e.g. Schruba et al. 2011) because we probe much larger spatial scales (13 arcsec $\sim$ 7.5 kpc for the BLUEDISK). Regarding depletion times, τ_{H2} decreases by a factor of $<$2, i.e. Σ_{H_2} drops faster than Σ_{SFR}, though we caution that a systematic change of X_{CO} with radius/metallicity can at least partly cancel this trend. On global scales, Boselli et al. (2014b) and Saintonge et al. (2011b) find a weak correlation between τ_{H2} and $\mu_\star$. Re-analysis of the COLD GASS data by Huang & Kauffmann (2014) also showed the lack of a significant trend between τ_{H2} and $\mu_\star$. The weak correlation is mostly driven by lower depletion times for lower $\mu_\star$ values and it disappears when H_2 is calculated from a metallicity-dependent X_{CO} factor (Boselli et al. 2014b). The atomic depletion time increases by a factor of 5, and the total gas depletion time increases by a factor of $\sim$2. The trend seen in H I is compatible with observations of nearby spirals (Bigiel et al. 2010a). The trend seen in H_2 is somewhat different from the molecular gas-rich, late-type discs studied in Leroy et al. (2013) for which depletion times are constant with radius and slightly lower in their centres. The discrepancy with our galaxies is probably due to the large scatter in our data and larger spatial scales probed.

Moreover, several trends appear when binning the profiles by their type (H I-rich/control). For the following discussion, we caution that we base our analysis on only 11 profiles (the good-quality HERA data). We identify behaviours as a trend if the average quantity in one category is outside of the range of radial distributions (i.e. the scatter, indicated as the hashed regions) in the other category. First, Σ_{H_2} seems to decrease faster with radius for the H I-rich galaxies. The trend is weaker but still present when correcting CO profiles for metallicity variations with radius. The H I profiles are flatter, resulting in comparable normalized total gas surface density profiles for the H I-rich and control galaxies. As a consequence, the molecular fraction also decreases faster with radius for the H I-rich galaxies. This is interesting because the H I-rich galaxies display steeper metallicity gradients across their stellar discs than the control galaxies overall (Carton et al. 2015). We further quantify this in Section 5.3.

The molecular depletion time is marginally higher in the control galaxies than in the H I-rich galaxies by a factor of $\sim$1.4, as noticed in Fig. 2 on global scales. The atomic depletion times increase faster for the H I-rich galaxies, again due to the H I profiles being relatively flatter in the outer parts, and the total gas depletion times are globally constant with radius, with an increase at larger radii for the H I-rich galaxies.

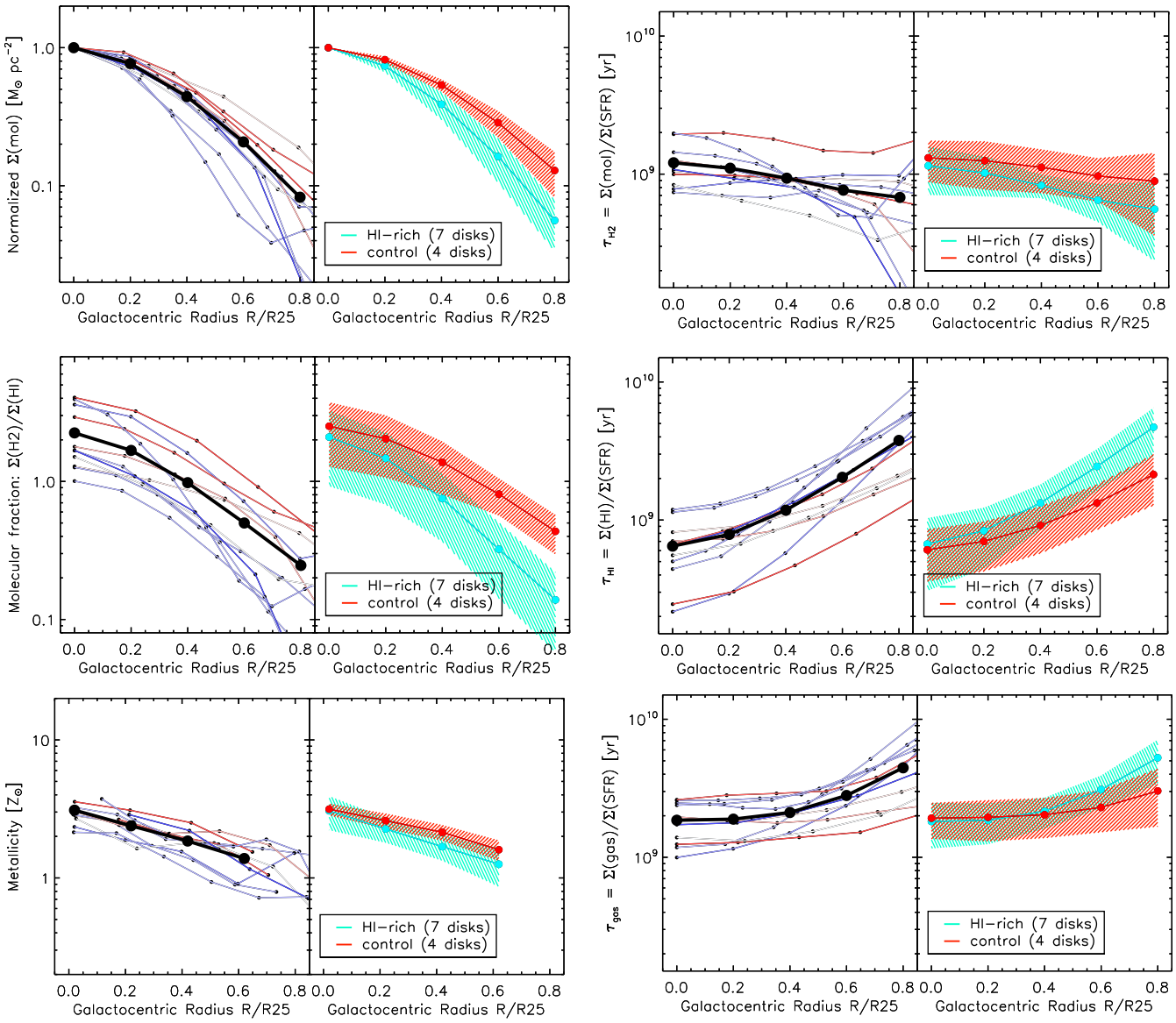

Figure 5. From top to bottom: (left column) normalized Σ_{H_2}, $\Sigma_{H_2}/\Sigma_{H\,I}$, and metallicity as a function of radius; (right column) molecular, atomic, and total gas star formation depletion times as a function of radius. For each quantity, panels on the left show profiles of all the mapped galaxies colour-coded upon the H I-rich/control classification. The black profile represents the mean profile of the sample. Panels on the right show mean profiles and their dispersion for galaxies classified as H I-rich (cyan)/control (red).

Although not shown in Fig. 5, we inspected results by binning our profiles by stellar mass or by presence of a bar in the galaxy. We found that several of the plots binned by stellar mass resemble those binned by colour because three of the four control discs are in the high-stellar mass range (ID9, ID10, ID11). The presence of a bar, identified in only three of our galaxies mapped in CO, does not seem to influence the radial behaviour of the quantities discussed (at the coarse resolution of our data).

Overall, the response from the inner half of the star-forming disc (within $0.5 \times R_{25}$) of the H I-rich galaxies to accretion seems non-existent or very slow. Only the molecular fraction and the molecular depletion time are marginally lower, while the atomic depletion time is marginally higher. In the outer parts of the disc, we find no evidence for a significantly elevated SFR or a detectable CO reservoir. Only the metallicity, decreasing below half-solar in some H I-rich galaxies, possibly translates in difficulties to detect CO beyond $\sim R_{25}$.

5.3 Extents and gradients comparison

We measure disc extents as the radius (distance from the disc centre) at which the CO surface density profile reaches 3 $M_\odot$ pc^{-2}, denoted R3(CO). The threshold is chosen based on data quality; below that value, the CO profiles are not reliable. For the H I and SFR profiles, we also choose a threshold of 3 $M_\odot$ pc^{-2} and 3×10^{-3} $M_\odot$ yr^{-1} kpc^{-2}, and we denote the corresponding radii R3(H I) and R3(SFR), respectively. Uncertainties on those derived quantities are estimated by iterating the process 100 times, varying data points of the profiles within their errors. This gives final uncertainties of ∼12 per cent. CO gradients are calculated as the difference in log of the surface density at $R = 0.5 \times R_{25}$ and $R = 0$.

Although we work with different threshold values and a smaller sample, the two upper, left-hand panels in Fig. 6 recover the results from Wang et al. (2013): H I-rich galaxies have more massive and more extended H I discs than the control sample. Our data points

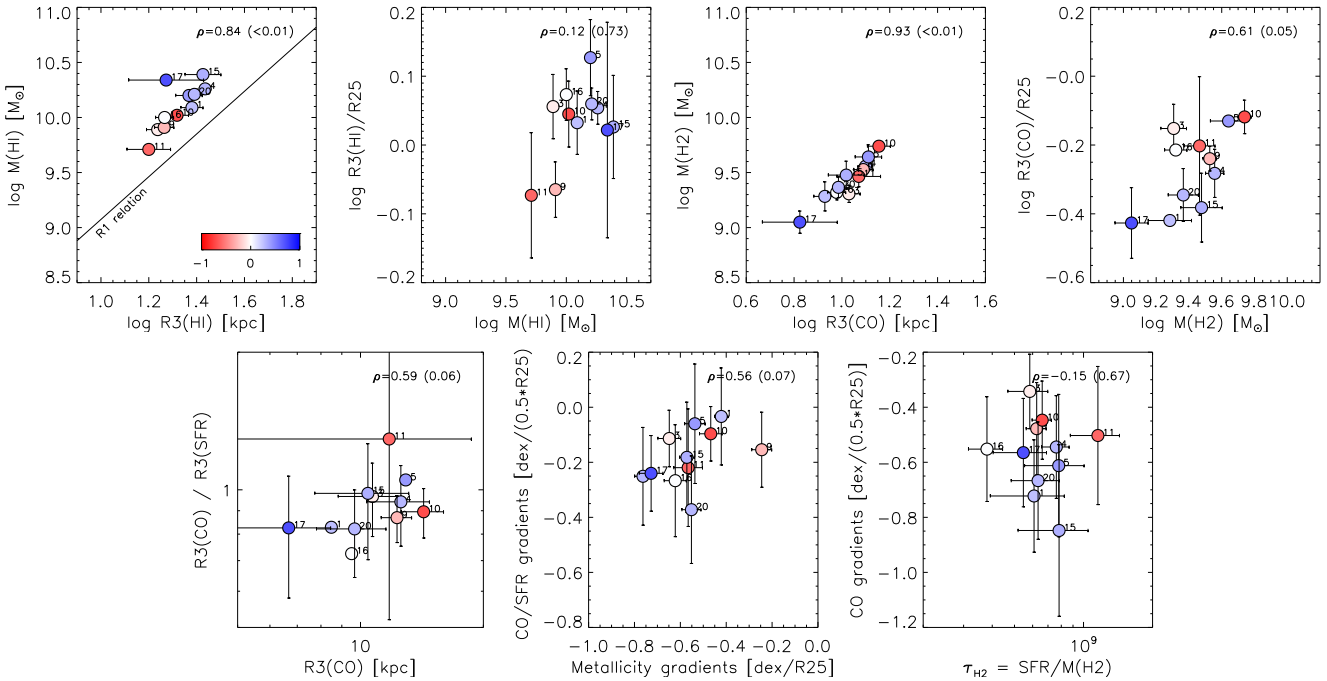

Figure 6. Comparison of surface density extents and gradients. R3 is the radius at which the surface density reaches 3 $M_\odot$ pc^{-2} for CO and H I, and 3×10^{-3} $M_\odot$ yr^{-1} kpc^{-2} for SFR. The line in the top, left-hand panel is the M(H I)–R1 relation found by Wang et al. (2013), i.e. measuring sizes where the H I surface density reaches 1 $M_\odot$ pc^{-2} instead of 3 $M_\odot$ pc^{-2} (hence R3<R1). The mean and standard deviation of each quantity are overplotted as crosses for the H I-rich and control samples. We also indicate Pearson correlation coefficients. Same colour-coding as in Fig. 1.

lie above the M(H I)-R1 relation because R3<R1. In the two upper, right-hand panels, we see that the most massive H_2 discs are also the biggest, with a tighter correlation than seen in H I, and, when normalized to R_{25}, the CO discs appear slightly more extended in the control sample, by ∼0.1 dex.

The lower, left-hand panel of Fig. 6 shows that the CO and SFR sizes are roughly compatible. CO is slightly more extended than the SFR in the largest CO discs, i.e. in the control discs. The two lower, middle panels show the CO/SFR gradients and CO gradients as a function of metallicity gradients and molecular depletion time, respectively. We find that, globally, the H I-rich galaxies have steeper CO gradients, steeper metallicity gradients, and marginally lower molecular depletion times, as discussed in Section 5.2. Note that even when correcting for metallicity effects (using a higher X_{CO} factor), weak trends remain present.

6 DISCUSSION

In this section, we aim to discuss our results on the two galaxy samples in the context of galaxy evolution. We find that the H I-rich galaxies differ from the control galaxies in being bluer, more gas-rich with lower H_2/H I ratios, and having slightly steeper CO and metallicity gradients and marginally shorter molecular gas consumption times.

Given the small stellar mass range probed by the BLUEDISK galaxies, variations in the sSFR values reflect variations about the main sequence of galaxies (plots in Fig. 2 look very similar when normalizing sSFR by the main-sequence values, hence we do not show them). Genzel et al. (2015) study $M(H_2)/M_\star$ and τ_{H2} as a function of redshift and offset from the main sequence. In particular, they find a decrease in τ_{H2} and an increase in $M(H_2)/M_\star$ with increasing offset from the main sequence (to high sSFR values), which is in agreement with the trends reported for our sample (at $z \simeq 0.03$) in Section 5.1. This supports findings at higher redshifts that gas fractions are higher in galaxies above the main sequence (Magdis et al. 2012; Scoville et al. 2016).

Analysis of global parameters in Section 5.1 tend to indicate that the H I-rich and control galaxies are mostly offset in the H I reservoir, and much less in H_2 mass or sSFR. As found in previous work, H I is not the main, direct fuel of the star formation activity in those galaxies. The larger H I reservoir in the H I-rich galaxies might argue for fresh accretion (Wang et al. 2015) with no time yet to transport the gas further in. This accreted atomic gas may at some point be converted into H_2 and then into stars. The time-scale of this process can be taken as the offset of the H I-rich and control galaxies in their τ_{gas} values, i.e. ∼5 Gyr. If the accretion is recent, those galaxies with large H I envelopes may not have had time to go back to equilibrium, and therefore the estimated time-scale is a lower limit. Even though the H I-rich galaxies are gas-rich, their normalized gas surface densities are below average, especially in the inner parts of the disc (Fig. 4). This may confirm that the gas has not progressed towards the inner parts yet and hence the growth of the disc is slow despite evidence for accretion. This picture is somewhat more secular than in starburst galaxies where elevated SFRs are due to efficient conversion of H I to H_2 and stars (e.g. Jaskot et al. 2015). The fact that the H I-rich galaxies in our survey appear blue because of metallicity rather than elevated SFR (Figs 1 and 2) is consistent with this secular evolution interpretation. The H I-rich/control offset may be interpreted as an evolutionary sequence and could also partly explain the large dispersions in the correlations found for larger galaxy samples.

Overall, with the BLUEDISK survey, we are looking at similar galaxies (same stellar mass, redshift) but in apparent different moments of their build-up (different gas budget), where the H I-rich galaxies have (recently) accreted atomic gas. Concerning the duty cycle of gas accretion events, in order to easily detect fluctuations in the

accretion histories, such fluctuations have to occur on time-scales similar to or longer than the time-scale to consume the excess of atomic gas (i.e. several Gyr). However, following the evolution of one group to the other is not trivial as galaxy evolution is a multiparameter problem and our sample is small. By analysing the stellar content of thousands of galaxies, Dressler et al. (2016) find that, at a given stellar mass, the same galaxies could have undergone very different star formation histories. They conclude that there is not one typical evolutionary track for a galaxy at a given mass, in line with our finding here. We can still speculate on how the H I-rich galaxies will evolve with time if they no longer accrete significant amounts of gas. For them to reach similar $M(\mathrm{H\,I})/M_\star$ levels as the control galaxies, they have to consume $\sim 1 \times 10^{10}$ $\mathrm{M}_\odot$, which corresponds to an increase in stellar mass of 25 per cent. With time (and in a closed box), their metallicities will also increase and their colours turn redder as the bulk of the stars become older. By that time, the main characteristics of the H I-rich galaxies will disappear and the H I-rich galaxies will look like control galaxies. On even longer time-scales, as those galaxies are isolated, their SFR will probably decrease due to strangulation (supply of cold gas halted) rather than removal of external gas (e.g. Peng, Maiolino & Cochrane 2015).

Within the H I-rich galaxies, we also find some scatter in the central H_2/H I values. ID4, ID16, ID20 have lower H_2/H I ratios than the other discs. Interestingly, these three galaxies show a clumpy morphology in optical images, and they also have an H I excess in their centres (Wang et al. 2014). Qualitatively, this is consistent with theoretical models by Krumholz, McKee & Tumlinson (2009) which suggest a clumping factor of unity for those discs. Clumpier H_2 distributions would dilute the surface density of molecular gas relative to $\Sigma_{\mathrm{H\,I}}$ in our beam. Additionally, in a clumpy medium, the radiation field pervades and is probably an important parameter in setting the atomic/molecular balance. Theoretical models also highlight the importance of metallicity in influencing the H I-to-H_2 transition (Krumholz et al. 2009; Sternberg et al. 2014). ID4, ID16, ID20 do not show lower central metallicities than the other H I-rich galaxies, hence, we do not expect metallicity to be responsible for their low H_2/H I ratios. The variations of the H_2/H I ratio, lower in the clumpy galaxies of the BLUEDISK survey and higher in the Sa/b galaxies, are also consistent with studies showing an evolution of the molecular fraction with morphological type (e.g. Young & Knezek 1989; Obreschkow & Rawlings 2009).

Concerning disc extents, Obreschkow et al. (2009) report, using the Millennium Simulation, a smooth evolution of the H I mass and disc radius with redshift, while molecular masses are higher and molecular discs smaller at high redshift due to increased pressure. For the BLUEDISK galaxies, we find in Section 5.3 that the least extended CO and SFR discs relative to R_{25} are those of the H I-rich galaxies ID1, ID15, and ID17. These three galaxies are grouped in the category of discs with H I excess between R_{25} and R1(H I) by Wang et al. (2014). Perhaps this surrounding H I gas will not be transported further in the disc and will participate in the growth of the CO disc from the outskirts.

7 SUMMARY

To shed light on the role of gas accretion in the evolution and growth of galaxies, the BLUEDISK survey has investigated optical and radio properties of 50 nearby disc galaxies. Among those, 25 have enhanced H I content and bluer discs than average for their stellar mass (Wang et al. 2013, 2014; Carton et al. 2015). The objective of this paper is to establish whether the H I-rich galaxies also have different molecular gas and star formation properties than the normal, control galaxies. We have observed the molecular gas tracer CO in 26 galaxies of the BLUEDISK survey and resolved emission in 15 of them, 11 of which are H I-rich galaxies and 4 of which are control galaxies.

Despite the excess of H I gas in the H I-rich galaxies, we find that the H I-rich and control galaxies have similar total molecular masses, $\sim 3 \times 10^9$ $\mathrm{M}_\odot$. H I-rich galaxies show marginally shorter molecular depletion times and longer gas (atomic and molecular) depletion times. The large atomic gas reservoir of the H I-rich galaxies may play a role in sustaining their SFR but does not imply a significant or systematic increase in the molecular gas mass or SFR.

We detect CO in radial profiles out to $\sim 0.7 \times R_{25}$. We compare those to radial profiles of H I, SFR, and metallicity. Besides higher molecular SFE and lower H_2/H I ratios in the centres of the H I-rich galaxies, the main differences between H I-rich and control galaxies lie in the outer parts of the disc: more atomic gas, less molecular gas, and lower metallicities. CO discs also appear slightly smaller in the H I-rich galaxies.

Signatures from atomic gas accretion on the inner disc and on the molecular gas properties are found almost inexistent. We conjecture that the excess H I gas of the H I-rich galaxies will be consumed and participate to the growth of the molecular disc. Comparing the relevant time-scales, we conclude that the conversion of this gas into H_2 and then into stars is a rather slow process ($\sim$5 Gyr). A secular evolution of the H I-rich galaxies into control galaxies is therefore expected.

ACKNOWLEDGEMENTS

We are grateful to Mei-Ling Huang for her help with the BLUEDISK SFR data. We would like to thank Barbara Catinella and Sacha Hony for careful reading of the manuscript and helpful comments, as well as David Elbaz and Adam Leroy for interesting discussions. We also thank the referee for a very constructive report. DC and FB acknowledge support from DFG grant BI 1546/1-1. JP acknowledges support from the CNRS program 'Physique et Chimie du Milieu Interstellaire' (PCMI). JMvdH acknowledges support from the European Research Council under the European Union's Seventh Framework Programme (FP/2007-2013)/ERC Grant Agreement nr. 291531. This work is based on observations carried out with the IRAM 30-m Telescope. IRAM is supported by INSU/CNRS (France), MPG (Germany) and IGN (Spain). This publication makes use of data products from the *WISE*, which is a joint project of the University of California, Los Angeles, and the Jet Propulsion Laboratory/California Institute of Technology, funded by the National Aeronautics and Space Administration.

REFERENCES

Bauermeister A., Blitz L., Ma C.-P., 2010, ApJ, 717, 323
Bigiel F., Blitz L., 2012, ApJ, 756, 183
Bigiel F., Leroy A., Walter F., Brinks E., de Blok W. J. G., Madore B., Thornley M. D., 2008, AJ, 136, 2846
Bigiel F., Leroy A., Walter F., Blitz L., Brinks E., de Blok W. J. G., Madore B., 2010a, AJ, 140, 1194
Bigiel F., Leroy A., Seibert M., Walter F., Blitz L., Thilker D., Madore B., 2010b, ApJ, 720, L31
Bolatto A. D., Wolfire M., Leroy A. K., 2013, ARA&A, 51, 207
Boselli A., Cortese L., Boquien M., 2014a, A&A, 564, A65
Boselli A., Cortese L., Boquien M., Boissier S., Catinella B., Lagos C., Saintonge A., 2014b, A&A, 564, A66
Carton D. et al., 2015, MNRAS, 451, 4729
Catinella B. et al., 2010, MNRAS, 403, 683

Catinella B. et al., 2013, MNRAS, 436, 34
Charlot S., Longhetti M., 2001, MNRAS, 323, 887
Chary R., Elbaz D., 2001, ApJ, 556, 562
Cormier D. et al., 2014, A&A, 564, A121
Dressler A. et al., 2016, preprint (arXiv:1607.02143)
Elbaz D. et al., 2007, A&A, 468, 33
Erb D. K., 2008, ApJ, 674, 151
Genzel R. et al., 2015, ApJ, 800, 20
Hopkins A. M., McClure-Griffiths N. M., Gaensler B. M., 2008, ApJ, 682, L13
Huang M.-L., Kauffmann G., 2014, MNRAS, 443, 1329
Jaskot A. E., Oey M. S., Salzer J. J., Van Sistine A., Bell E. F., Haynes M. P., 2015, ApJ, 808, 66
Kennicutt R. C., Jr,1983, ApJ, 272, 54
Krumholz M. R., McKee C. F., Tumlinson J., 2009, ApJ, 693, 216
Leroy A. K., Walter F., Brinks E., Bigiel F., de Blok W. J. G., Madore B., Thornley M. D., 2008, AJ, 136, 2782
Leroy A. K. et al., 2009, AJ, 137, 4670
Leroy A. K. et al., 2013, AJ, 146, 19
Lisenfeld U. et al., 2011, A&A, 534, A102
Magdis G. E. et al., 2012, ApJ, 760, 6
Martin D. C. et al., 2005, ApJ, 619, L1
Mateos S. et al., 2012, MNRAS, 426, 3271
Moran S. M. et al., 2010, ApJ, 720, 1126
Moran S. M. et al., 2012, ApJ, 745, 66
Noeske K. G. et al., 2007, ApJ, 660, L43
Obreschkow D., Rawlings S., 2009, MNRAS, 394, 1857
Obreschkow D., Croton D., De Lucia G., Khochfar S., Rawlings S., 2009, ApJ, 698, 1467
Peng Y., Maiolino R., Cochrane R., 2015, Nature, 521, 192
Saintonge A. et al., 2011a, MNRAS, 415, 32
Saintonge A. et al., 2011b, MNRAS, 415, 61
Sancisi R., Fraternali F., Oosterloo T., van der Hulst T., 2008, A&AR, 15, 189
Schruba A. et al., 2011, AJ, 142, 37
Scoville N. et al., 2016, ApJ, 820, 83
Sternberg A., Le Petit F., Roueff E., Le Bourlot J., 2014, ApJ, 790, 10
Wang J., Overzier R., Kauffmann G., von der Linden A., Kong X., 2010, MNRAS, 401, 433
Wang J. et al., 2013, MNRAS, 433, 270
Wang J. et al., 2014, MNRAS, 441, 2159
Wang J. et al., 2015, MNRAS, 453, 2399
Wang J., Koribalski B. S., Serra P., van der Hulst T., Roychowdhury S., Kamphuis P., Chengalur J. N., 2016, MNRAS, 460, 2143
Wright E. L. et al., 2010, AJ, 140, 1868
Young J. S., Knezek P. M., 1989, ApJ, 347, L55

APPENDIX: IRAM DATA OF THE BLUEDISK GALAXIES

We present SDSS images and the IRAM data of the BLUEDISK galaxies in Fig. A1 for the galaxies mapped with HERA and in Fig. A2 for the galaxies observed with EMIR. SDSS images were downloaded from the DR7 Data Archive Server (http://das.sdss.org/www/html/). Images are 1.6 arcmin × 1.6 arcmin in size. In Fig. A1, the HERA coverage (1.2 arcmin × 1.2 arcmin) and beam size (11 arcsec at 230 GHz) are drawn on top. In Fig. A2, the EMIR beam at 115 GHz (22 arcsec) is drawn on top of the image. All IRAM spectra have spectral resolution 15.6 km s^{-1}. The vertical lines show the optical centre (plain red), the CO centre (plain blue), and the width of the CO line (dashed blue). Note that the width indicated for the HERA spectra is only shown for comparison, it is computed for each pixel individually in these resolved maps. Spectra are labelled (HI) for the H I-rich glaxies, (C) for the control galaxies, (E) for excluded galaxies, and (P) for poor quality.

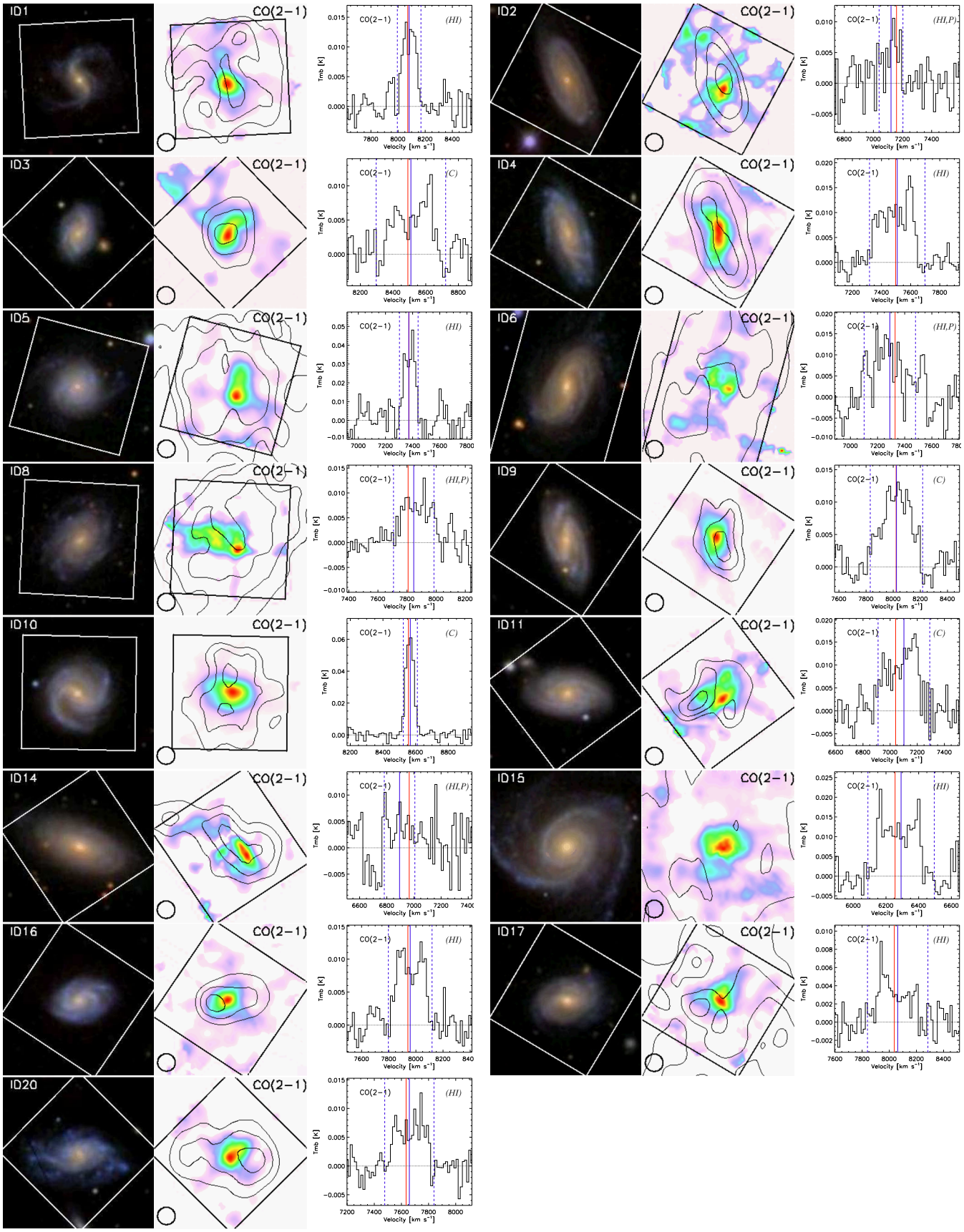

Figure A1. SDSS 3-colour images (*r*, *g*, *i* bands), HERA CO(2–1) intensity map with H I contours (levels at roughly 50 per cent, 70 per cent and 90 per cent of the emission peak), and spectrum within a central aperture of diameter 22 arcsec (EMIR beam size at the observed frequency of 112 GHz).

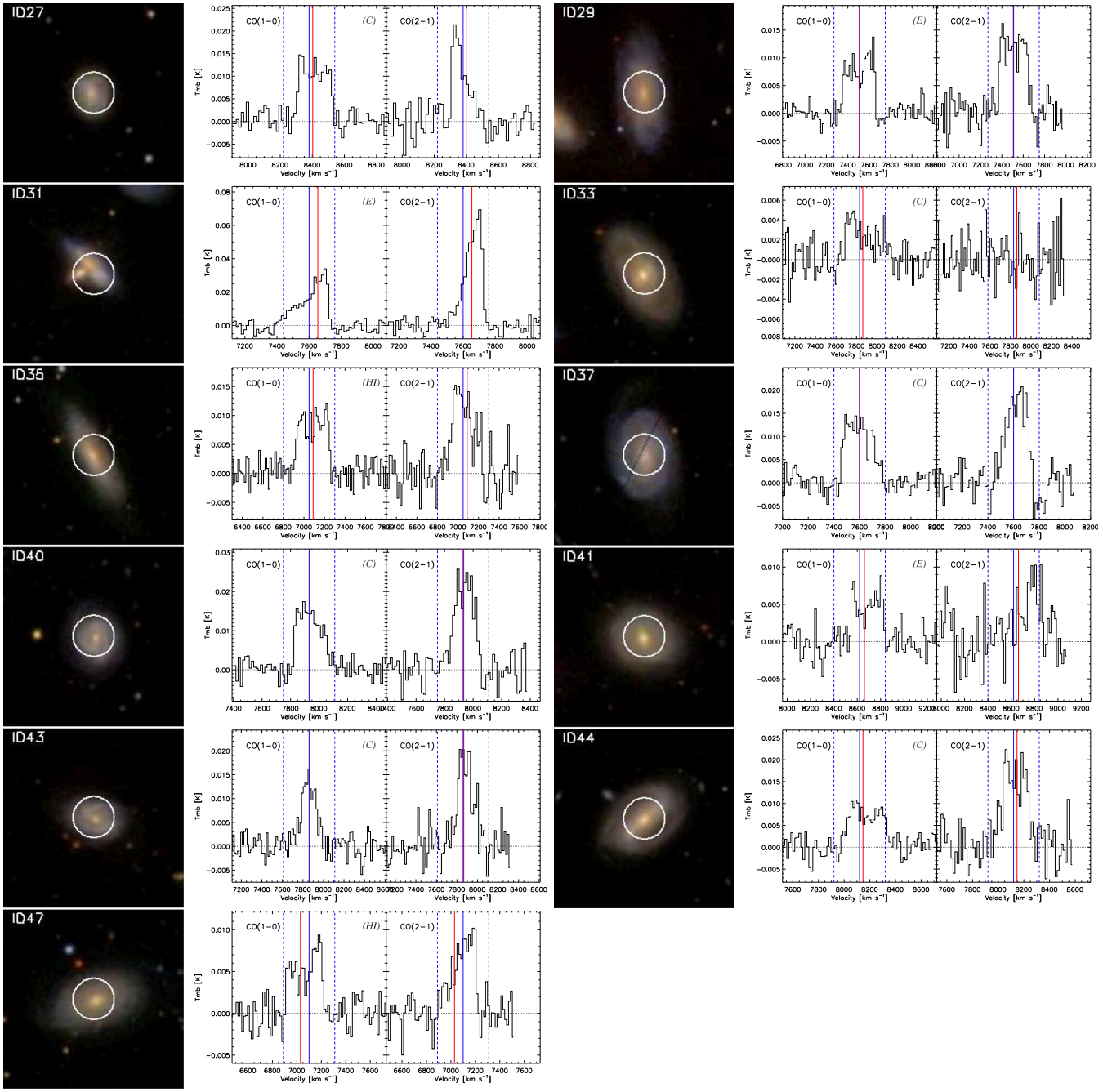

Figure A2. SDSS 3-colour images (*r*, *g*, *i* bands) of the control galaxies and their EMIR spectra of CO(1–0) and CO(2–1).

This paper has been typeset from a TEX/LATEX file prepared by the author.